Anomalous resonance in a nanomechanical biosensor

Amit K. Gupta*†, Pradeep R. Nair*†, Demir Akin*†‡, Michael R. Ladisch‡, Steve Broyles§, Muhammad A. Alam*†, and Rashid Bashir*†‡¶

*Birck Nanotechnology Center, †School of Electrical and Computer Engineering, ‡Weldon School of Biomedical Engineering, and §Department of Biochemistry, Purdue University, West Lafayette, IN 47907

The decrease in resonant frequency ($-\Delta\omega_r$) of a classical cantilever provides a sensitive measure of the mass of entities attached on its surface. This elementary phenomenon has been the basis of a new class of bio-nanomechanical devices as sensing components of integrated microsystems that can perform rapid, sensitive, and selective detection of biological and biochemical entities. Based on classical analysis, there is a widespread perception that smaller sensors are more sensitive (sensitivity $\approx -0.5\omega_r/m_C$, where m_C is the mass of the cantilever), and this notion has motivated scaling of biosensors to nanoscale dimensions. In this work, we show that the response of a nanomechanical biosensor is far more complex than previously anticipated. Indeed, in contrast to classical microscale sensors, the resonant frequencies of the nanosensor may actually decrease or increase after attachment of protein molecules. We demonstrate theoretically and experimentally that the direction of the frequency change arises from a size-specific modification of diffusion and attachment kinetics of biomolecules on the cantilevers. This work may have broad impact on microscale and nanoscale biosensor design, especially when predicting the characteristics of bio-nanoelectromechanical sensors functionalized with biological capture molecules.

nanocantilevers | nanotechnology | protein adsorption | virus detection

Table 1. List of symbols used and their definitions

Symbol	Definition
ω_r	First natural frequency
k_C	Linear spring constant
ω_r^A	First natural frequency after protein layer attachment
ω_r^B	First natural frequency after target analyte capture
m_C	Effective mass of the cantilever
m_A	Effective mass of the protein layer
m_B	Mass of the target analyte biomolecule
$\Delta\omega_r^A$	Change in resonant frequency after protein layer attachment
$\Delta\omega_r^B$	Change in resonant frequency after target analyte biomolecules capture
k_{C+A}	Linear spring constant of the cantilever after protein layer attachment
L_C	Length of cantilever beam
W_C	Width of cantilever beam
t_C	Thickness of cantilever beam
t_A	Thickness of protein layer
A_C	Surface area of cantilever beam
$L_{C,T}$	Transition length of cantilever that predicts reversal of sign of $\Delta\omega_r^A$ after protein layer attachment
$t_{C,T}$	Transition thickness of cantilever that predicts reversal of sign of $\Delta\omega_r^A$ after protein layer attachment
E_{comp}	Young's modulus of the composite protein/cantilever layer
ρ_{comp}	Density of the composite protein/cantilever layer
ρ_C	Density of the cantilever material
ρ_A	Density of the protein layer
k_B	Boltzmann's constant
T	Temperature of surrounding medium
B	Measurement bandwidth
Q	Unloaded quality factor of cantilever beam
$\langle\hat{A}\rangle$	Square root of the mean-square amplitude of the vibration of the cantilever

Vibrating cantilever beams have been used to detect ultrasmall masses, ranging from femtogram down to the zeptogram range (1–6). This principle of detection is simple: The first natural frequency of a unloaded cantilever is $\omega_r = (k_C/m_C)^{1/2}$, where k_C and m_C are the linear spring constant and effective mass of the cantilever, respectively (see Table 1 for list of symbols used). The functionalization or capture of proteins on the cantilever shifts $\omega_r \rightarrow \omega_r^A$, as adsorbed molecules change the spring constant by k_A and increase the mass by m_A. The capture of the analyte biomolecule by the receptor proteins further increases the mass by m_B and decreases the resonant frequency from $\omega_r^A \rightarrow \omega_r^B$, such that $\Delta\omega_r^B = \omega_r^B - \omega_r^A$ registers the presence or absence of captured particles, for example, bacteria (1) or viruses (2–4).

Classical theory of resonators suggests that scaling down the area (A_C) of a cantilever would reduce m_C and m_A and therefore allow detection of smaller concentrations or amounts of biomolecules, whereas scaling down the thickness (t_C) decreases the resonant frequencies to be within measurable range. Specific capture of antigens requires attachment of receptor molecules such as antibodies (Abs) (4, 7) whose thickness (t_A) may be comparable with nanoscale cantilevers ($t_A \sim t_C$). As such, the mechanical properties of nano-cantilevers, coated with receptor molecules, can be significantly different from their bulk counterparts. Earlier works have described the alteration of the spring constant, k_C, of microscale-thick cantilever beams due to changes in stress on one side of the cantilever (8, 9), but the effect of the mass of the adsorbed layer was negligible in those experiments because the mass of cantilever, m_C, was much greater than mass of the adsorbed layer, m_A. The influence of the mass and the spatial distribution of proteins on nanoscale sensor have never been studied explicitly and remains a poorly understood phenomenon (10). In this work, we use detailed vibration measurements and fluorescence microscopy to establish that the protein attachment increases with cantilever size, and this size-dependent capture of receptor density in turn, is reflected in

anomalous increase in frequency for a certain class of cantilevers. We use a simple diffusion-limited capture model to interpret these phenomena (i.e., increased protein capture and increase in frequency after protein absorption), neither of which are anticipated from traditional considerations. Our results highlight subtle interplay of mechanical effects due to protein coverage on nanoscale-thick sensors and should provide guidelines for design of cantilever sensors and arrays in integrated microfluidic devices.

Results and Discussions

Silicon cantilever beams with length $L_C \sim$ 3–5 μm, width $W_C \sim$ 1.4–1.5 μm and thickness $t_C \sim$ 30 nm were used for the resonant detection of proteins and vaccinia virus particles. The "unloaded" resonant frequency (ω_r) was first measured in air by using a laser Doppler vibrometer. Next, three different receptor (Ab) attachment schemes were used (on three different chips; see *Materials and Methods*) to functionalize the cantilevers. These three schemes are shown in Fig. 1 a–c. Scheme 1 was used to perform the selective
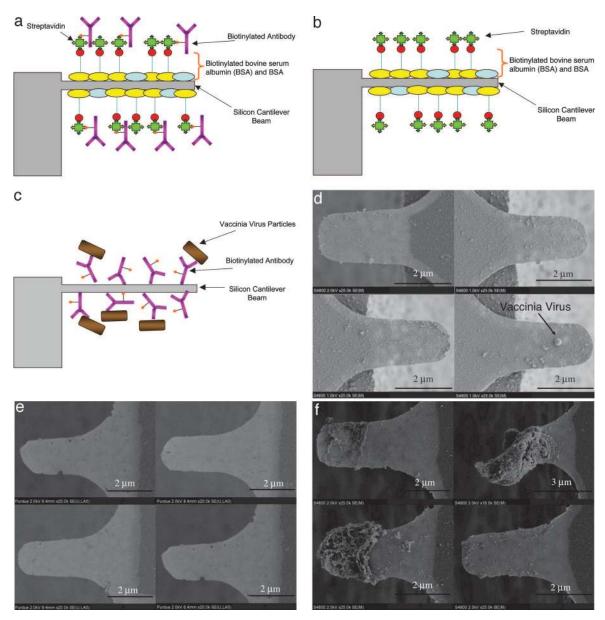
Fig. 1. Protein attachment schemes and the corresponding images of the functionalized cantilevers. (*a–c*) Schematic diagrams depicting protein attachment for schemes 1 (*a*), 2 (*b*), and 3 (*c*). (*d–f*) Collection of field emission scanning electron micrographs representing the interaction of a mixture of virus particles with protein-coated cantilever beams using schemes 1 (*d*), 2 (*e*), and 3 (*f*). Scheme 1 shows the capture of vaccinia virus in some cases, whereas cantilevers with scheme 2 have no capture at all. Scheme 3 shows significant nonspecific capture. Note that in *f*, the top right cantilever is bent severely because of excessive nonspecific binding.

capture, and schemes 2 and 3 were used as controls. The protein-coated cantilever beams were dried by using critical point drying (CPD), and the resonant frequencies ($\Delta\omega_r^A$) were measured in air by using the laser Doppler vibrometer. Subsequently, the dry protein-coated cantilever beams were immersed in PBS solution (pH 6.3) to reactivate the Ab molecules and then treated with a mixture of antigens. Cantilevers were then dried, and the loaded resonant frequencies ($\Delta\omega_r^B$) were measured again in air.

In addition to the measurement of resonant frequencies, the cantilevers were imaged by using a field emission scanning electron microscope (see Fig. 1 *d–f*). The composite protein layer (scheme 1) captured viruses in some cases, whereas the control BSA layer-coated (scheme 2) cantilevers did not capture virus particles. The Ab-coated cantilever beams without BSA (scheme 3), in turn, seemed to capture a large number of particles/aggregates as shown in Fig. 1*f*. The BSA layer, known to function as a blocking layer, prevented the significant capture of virus particles for schemes 1

and 2, whereas the Ab-alone-coated cantilever beams (scheme 3) nonspecifically captured a relatively larger number of aggregates and particles rather nonselectively.

Table 2 summarizes the mechanical parameters of the cantilever beam at the various stages of the biosensor analysis for scheme 1. The calculated minimum detectable frequency shift (Eq. **4** in supporting information, which is published on the PNAS web site) is also included for each of the two particular mass measurements of the protein layers and the viruses (the range in the unloaded measured ω_r is attributed to variation in the length of the cantilevers). Table 2 shows that after the attachment of the proteins, $\Delta\omega_r^A = \omega_r^A - \omega_r$, may either decrease (Fig. 2*a*) or increase (Fig. 2*b*), an anomalous result unexpected from traditional considerations (11). Regardless of the initial trend after protein attachment, however, Table 2 and Fig. 2 show that $\Delta\omega_r^B = \omega_r^B - \omega_r^A$ stayed within the measurable range (within 2×) of the minimum detectable resonant frequency shift or decreased after capture of viruses (values indi-

Table 2. Summary of mechanical parameters of cantilever beams at various stages of the biosensing analysis, in which protein attachment scheme 1 was used

Cantilever number	L_C, length of cantilever, μm	W_C, width, μm	ω_r, unloaded natural frequency, MHz	Unloaded quality factor	k_C, unloaded linear spring constant, N/m	k_{C+A}, spring constant after composite protein attachment, N/m	$\Delta\omega_r^A$, measured change in resonant frequency after composite protein attachment, kHz	Calculated minimum detectable frequency shift to measure composite protein attachment, kHz	$\Delta\omega_r^B$, measured change in resonant frequency after virus capture, kHz	Calculated minimum detectable frequency shift to measure virus capture, kHz
SE_N1	3.1	1.7	2.407	7.28	0.0180	0.0160	−376	52	15	50
SE_N6	3.0	1.7	2.161	8.38	0.0173	0.0190	−236	47	−56	38
SE_N7	2.8	1.8	2.439	6.25	0.0142	0.0160	−87	64	−63	54
SE_N2a	2.8	1.6	2.237	5.88	0.0110	0.0160	−179	72	−27	45
SE_N3	2.9	1.6	2.246	6.32	0.0125	0.0162	−123	65	76	47
SE_N4a	2.5	1.6	3.242	13.05	0.0366	0.0281	−233	32	31	38
S5_N1a	3.4	1.5	2.633	6.11	0.0173	0.0220	−97	69	−67	51
S5_N2a	3.3	1.5	2.751	7.70	0.0232	0.0320	−195	57	−129*	35
S5_N4	3.3	1.4	2.146	4.89	0.0114	0.0197	−233	70	−66*	31
S5_N6a	3.1	1.4	2.930	6.87	0.0227	0.0330	−223	68	−112*	39
S5_N2b	4.3	1.5	1.227	7.95	0.0085	0.0094	112	25	−43	27
SE_N4b	3.1	1.8	1.831	8.05	0.0138	0.0165	82	49	−17	44
SE_N5	2.8	1.6	2.363	9.77	0.0201	0.0202	324	42	−66	49
S5_N5	3.3	1.4	1.767	7.23	0.0131	0.0202	55	39	−51	27
SE_N2b	3.2	1.7	1.933	10.17	0.0195	0.0193	108	38	−484*	41
S5_N1b	4.3	1.3	1.278	5.92	0.0062	0.0114	81	34	−71*	22
S5_N3	5.0	1.5	1.264	8.23	0.0091	0.0133	132	24	−58*	21
S5_N5b	4.5	1.5	1.256	6.28	0.0069	0.0123	633	32	−132*	45
S5_N6b	4.5	1.7	1.309	6.57	0.0076	0.0114	49	32	−104*	23
S5_N7	4.7	1.3	1.300	5.91	0.0072	0.0133	28	35	−60*	20

Lengths and widths were obtained through measurements using field emission scanning electron micrographs. Measured changes in resonant frequency after the virus capture step marked with asterisks are two times larger than the calculated minimum detectable frequency shift.

cated with asterisks in Table 2), consistent with classical predictions. Hence, the virus capture served as a control indicating that the resonant frequency decreases, as expected, when a point mass is added to the cantilever.

The puzzle of increase or decrease of resonant frequency after attachment of proteins requires a careful analysis. Because

$$\omega_r^A = \sqrt{\frac{k_{C+A}}{m_C + m_A}},$$

where k_{C+A} is the effective spring constant of the cantilever after protein molecule attachment, the resonant frequency could increase or decrease depending on whether the overall change in the spring constant due to the protein layers is larger than the effective added mass of the protein molecules or vice versa. Assuming that the cantilever front and back surface is uniformly coated with proteins, the net stress on the beam would be negligible. We assume a thickness of 50 nm for the proteins, estimated from the known sizes of an Ab IgG molecule (23.5×2.5 nm^2) (12), a BSA molecule (14×4 nm^2) (13), and a streptavidin molecule (5.8×5.4 nm^2) (14)
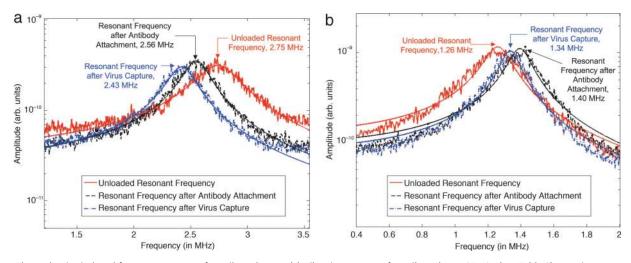

Fig. 2. Thermal noise-induced frequency spectra of cantilever beams. (*a*) Vibration spectra of cantilever beam S5_N2a (see Table 2) at various stages of the biosensor analysis showing the resonant frequency decreasing after the Ab sandwich attachment (scheme 1) and after the antigen capture. (*b*) Vibration spectra of cantilever beam S5_N3 (see Table 2) at various stages of the biosensor analysis showing the resonant frequency increasing after the Ab sandwich attachment and decreasing after the antigen capture. [Reproduced with permission from Gupta *et al.* (11) (Copyright 2005, IEEE).]
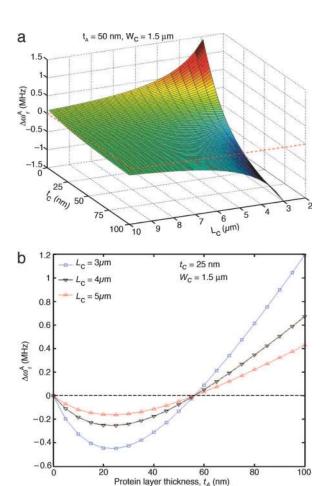
Fig. 3. Calculations of resonant frequencies. (*a*) Analytical calculations (using an idealized model of a rectangular shaped cantilever beam) showing the resonant frequency shifts ($\Delta\omega_r^A$ = loaded minus the unloaded resonant frequency) after protein attachment, displayed in a 3D plot as a function of cantilever beam thickness, t_C, and cantilever beam length, L_C, for a protein layer thickness, $t_A = 50$ nm, and a cantilever beam width, $W_C = 1.5\ \mu$m. (*b*) Analytical calculations (using an idealized model of a rectangular cantilever beam) showing the resonant frequency shift as a function of protein layer thickness for different cantilever beam lengths (with $t_C = 25$ nm and $W_C = 1.5\ \mu$m). The observed experimental results can only be explained by the trends in *b* where changes in protein thickness can result in an increase or decrease of the resonant frequency.

that were used in scheme 1. We then used the method of transformed cross-section to estimate the Young's modulus of the protein/cantilever structure (see supporting information) (15). We used a value of 1 GPa for the Young's modulus of the protein layer (16, 17) and 1.22×10^3 kg/m^3 for density of the protein layer (18). The Young's modulus for ultrathin silicon cantilever beams used in these calculations was 70 GPa (19), and the density of silicon used was 2.33×10^3 kg/m^3 (20). By using these values, one may then estimate the minimum detectable frequency shifts (see supporting information).

For our (presumably) uniformly coated cantilevers with thickness t_C and protein stack thickness $t_A \sim 50$ nm, the classical analytical model predicts reversal in the sign of $\Delta\omega_r^A$ ($= \omega_r^A - \omega_r$) with transition thickness of $t_{C,T} \sim 20$ nm, as shown in the 3D plot of Fig. 3*a*. Based on this calculation, we estimate that t_C should vary by as much as 50% to explain the changes in resonant frequency shifts observed in Table 2. However, detailed ellipsometer measurements on the starting silicon-on-insulator layer that formed the cantilever beam indicated that the thickness varied by only ±5.3% across the wafer. Therefore, thickness variation of the cantilever beam cannot cause the frequency shift reversal. The analytical calculations in Fig.

3*a* also show that the change in resonant frequency is always either negative or positive, independent of L_C for a given t_C and t_A; yet from the measured values reported in Table 2, L_C appears to be the most dominant indicator of the frequency reversal effect with transition length of approximately $L_{C,T} \sim 3\ \mu$m.

Remarkably, the classical model does offer a resolution of the puzzle if for some reason the thickness of the adsorbed protein (t_A) would scale with the length of the cantilever (L_C). Fig. 3*b* also shows the calculated variation in resonant frequency shift as a function of protein layer thickness for different cantilever lengths, with $t_C \sim 25$ nm. These analytical calculations show that if the longer cantilevers have a thicker protein layer, then the resonant frequency would increase as compared with a shorter cantilever, which would have a thinner protein layer. We also note that small changes in the protein layer thickness can cause the $\Delta\omega_r^A$ to change directions. For a 25-nm-thick cantilever, the frequency reversal occurs at critical thickness of $t_{A,T} \sim 56$ nm, and this thickness appears to be independent of the length of the cantilever, L_C.

To explore the hypothesis that thickness of the receptor protein changes with cantilever length, we then used a previously undescribed approach based on fluorescence microscopy to confirm our hypothesis. The intensity of the fluorescence signal from the secondary Abs, binding to the primary Abs and proteins used in scheme 1, was used as a signal to profile the spatial distribution of the proteins attached on the cantilever beam surfaces. To reduce cross-reactivity, the secondary (probe) Abs have to be chosen carefully. In scheme 1, the two main proteins used were biotinylated BSA and biotinylated Ab to vaccinia virus (rabbit source). The secondary Ab to BSA used was FITC-conjugated chicken anti-BSA. The secondary Ab to the rabbit vaccinia virus biotinylated Ab used was goat TRITC-conjugated anti-rabbit IgG. Fig. 4*a* shows the schematic of the binding of the labeled secondary Abs to the proteins used in scheme 1. Fluorescent images of the cantilevers with varying dimensions ranging from 3 to 100 μm in length and 1.5 to 9 μm in width were taken. Fig. 4*b* shows a black-and-white image of FITC filter fluorescent image of three cantilevers in the same field of view clearly showing that the brightness increases with length of the cantilever. Fig. 4*c* displays the results of the experimental analysis where each point in the plots is the mean intensity from each of the cantilever beams, and the smallest cantilevers are the same sizes used for the data in Table 2. Each experimental data point in Fig. 4*c* is an average from at least three different cantilever beams of approximately the same size. The mean fluorescence intensity can be correlated to the protein density (total mass/area of analysis) on the cantilever. The results clearly show that the tip region has more proteins as compared with the base region of the cantilevers, and hence there is an increase in the average fluorescence of the longer cantilevers as compared with the shorter ones. We also observed that the fluorescence at the tip region increases as the cantilever length increases.

To establish the physical basis of this unexpected phenomenon (i.e., higher protein density on longer cantilevers), we explored the kinetics of protein attachment onto the cantilever surface by a reaction–diffusion model (see details in *Materials and Methods*). We assumed instantaneous protein adsorption and neglected postattachment diffusion on the cantilever surface. We also assumed that the protein relaxation time is significantly smaller than the diffusion time (21). In this case, the steady-state density distribution is dictated by the kinetics of adsorption. The diffusion equation (Eq. **2** in *Materials and Methods*) was solved numerically in three dimensions for the same dimension cantilevers shown in Fig. 4*b*. We assumed infinite reaction rate at the cantilever surface and bulk protein concentration several micrometers away from the adsorbing surfaces. The time-integrated flux on the cantilever surface for a short duration is proportional to the steady-state adsorbed protein density. In Fig. 4 *c* and *d*, the simulation results clearly indicate that the protein density along the cantilevers increases for longer cantilevers as compared with the smaller ones,
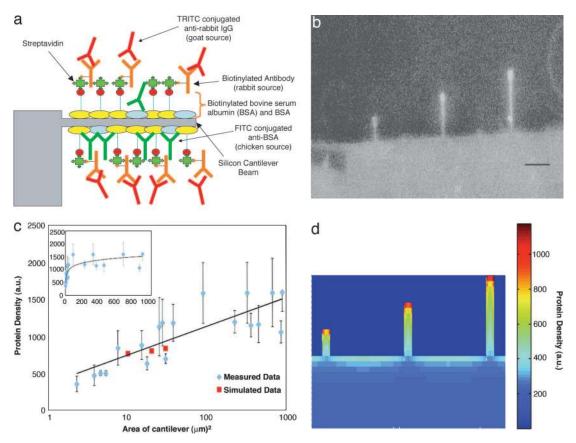
Fig. 4. Area-dependent protein adsorption. (*a*) Schematic diagram depicting the methodology of the specific binding of the secondary Abs to the proteins used in scheme 1. (*b*) Photomicrograph of fluorescently labeled (FITC; green) Ab to BSA attached to varying sized cantilever beams clearly showing an increase in fluorescent intensity for longer cantilevers. (Scale bar, 5 μm.) (*c*) Semilog plot showing the measured average fluorescence intensity from the secondary Abs to the proteins used in scheme 1 as a function of cantilever beam area. (*Inset*) The same parameters in the linear scale. The squares indicate the simulated protein density at the tip of the cantilevers shown in *b*. The simulated value of the shortest cantilever beam ($L_C = 5$ μm in *b*) was normalized with the measured value of the same length scale, the remaining two simulated lengths ($L_C = 10$ and 15 μm) were scaled by the same factor, and then all three simulated values were plotted with the measured data. (*d*) Simulated protein density distribution on the adsorbing cantilever surfaces. The density reaches a maximum for the longer cantilever. The monotonic increase in density with the cantilever length is due to the competitive attachment of protein among the adsorbing surfaces. Simulated protein density at the tip of the cantilevers is in excellent agreement with the experimental results. The dimensions in this simulation are the same as the cantilevers shown in *b*.

which is in complete agreement with the data based on fluorescence microscopy. This rather unexpected result is readily explained in terms of competitive protein attachment among the adsorbing sensor surfaces. Because of its large area, the base region can competitively capture proteins from the vicinity of the cantilevers. This phenomenon results in a reduction in the adsorbed protein density for smaller cantilevers, and the density profile along the cantilevers increases monotonically to a maximum at the tips. The trend would be reversed if competition with the base were eliminated (10), because the geometry of diffusion would favor smaller cantilevers compared with larger ones (22). We also note that these counterintuitive effects were only discovered when measuring the resonant frequencies of nanoscale-thick cantilevers.

Vibrating cantilever beam and other resonant sensors require the capture of the target at the vibrating end for maximum sensor response. The higher (diffusion-assisted) capture efficiency of proteins by the tip region of the cantilever has a favorable consequence for design of resonant sensors, i.e., the corresponding receptor profile maximizes the capture of analyte biomolecules at regions where the measurement change in resonant frequency would be the maximum. Our results imply the possibility of a "maskless" means of modulating the protein density based on the layout and dimensions of the cantilevers, obviating the need for complicated techniques for patterning of proteins at desired regions. Similarly, for a double-clamped suspended beam, the highest

protein density would be in the middle of the beam, resulting in the maximum response upon capture of target molecules. In addition, the ability to deposit different densities of proteins as a function of dimensions and geometry on suspended microscale and nanoscale structures can have an impact on the design of protein arrays and other sensor types.

Conclusions

This work represents an important step toward understanding the mechanics of protein attachment on nanoscale cantilever sensors in microfluidic devices. The attached protein density was shown to be a function of the area of the cantilever sensor, a phenomenon accentuated and found only because of the resonance measurements of the nanoscale-thick cantilevers. It should be noted that certain dimensions and geometry of the cantilevers could have a higher average density of proteins, resulting in an increase in the effective spring constant and a corresponding increase in resonant frequency upon binding of proteins of certain thicknesses. Hence, the change in the average protein density as a function of length (and thus dimensions) of the cantilever needs to be understood when designing cantilever array based nanomechanical sensors. Further exploration of the dependence of protein density on more complicated structures such as double-clamped beams, U- and V-shaped cantilevers, cantilevers with paddles at the free end, etc., is needed.

Materials and Methods

Cantilever Fabrication and Mechanical Characterization. In the present study, arrays of silicon cantilever beams were fabricated by using a combination of wet and dry etching processes as described (2). After fabrication, the cantilever beams were cleaned by using a standard piranha solution (hydrogen peroxide and sulfuric acid in a 1:1 ratio), rinsed in deionized water, immersed in ethanol, and then dried by using a CPD system. The thermal and ambient noise-induced frequency spectra of the cantilever beams were measured by using a microscope scanning laser Doppler vibrometer (MSV-300 from Polytec PI, Hopkinton, MA) under ambient air conditions. To obtain the resonant frequency and quality factor, the measured thermal spectra of the cantilevers were fitted to the amplitude response of a simple harmonic oscillator (23). The measured resonant frequencies of the cantilever beams were in the 1- to 2-MHz range with quality factor of ≈5–7. The cantilever beams were calibrated by obtaining their spring constant using the Sader method (24). This method requires the knowledge of the cantilever plan dimensions, unloaded resonant frequency, quality factor, and the density of the medium (air in this case) in which the cantilever is immersed.

Theoretical Protein Adsorption Model. The kinetics of Ab attachment on cantilever surface was explored by using the reaction–diffusion model. The rate of conjugation between the Abs on a cantilever surface and the secondary Abs in the solution, assuming irreversible conjugation, is given as (21)

$$\frac{dN}{dt} = k_F\Phi(N)\rho_s,\qquad [1]$$

where N is the number of conjugated protein pairs, $\Phi(N)$ (in general, a polynomial in N) gives the fraction of area available for conjugation, k_F is the reaction constant, and ρ_s is protein density at the cantilever surface.

We assume that the reaction is diffusion limited and that the protein relaxation time is significantly smaller than the diffusion time. In this case, the steady-state density is determined by initial adsorption kinetics. The diffusion of protein molecules to the cantilever surface is given as

$$\frac{d\rho}{dt} = D\nabla^2\rho,\qquad [2]$$

where ρ is concentration and D is diffusion constant of protein molecules in the solution. The diffusion coefficient of FITC-labeled protein molecules was obtained from a different experiment ($D =$ 10^{-6} cm^{-2}/s). Eq. **2** is solved numerically in three dimensions by the finite volume method assuming infinite conjugation rate at the cantilever surface and bulk protein concentration several micrometers away from the adsorbing surfaces. The time-integrated flux on the cantilever surface for short duration is proportional to the steady-state adsorbed protein density.

Protein Attachment Method. For the selective capture experiment, cantilevers were cleaned in a solution of standard piranha (H_2O_2:H_2SO_4 = 1:1 in vol.), rinsed in deionized water, immersed in ethanol, dried by using a CPD system, and then measured to obtain the unloaded resonant frequencies. For protein attachment scheme 1 (25) (see Fig. 1a), the cantilevers were then treated with 15 μl of biotinylated BSA (1.5 mg/ml) for 30 min, followed by a rinse in PBS (pH 6.3) for 5 min. The cantilevers were then treated with 15 μl of streptavidin (United States Biological, Inc., Swampscott, MA) (5 mg/ml) for 15 min, rinsed in PBS-Tween 20 (0.05%) for 5 min to remove the excess streptavidin, and then treated with 15 μl of biotinylated Ab to vaccinia virus (United States Biological, Inc.) (5 mg/ml) for 15 min. After a rinse in PBS-Tween 20 for 5 min, the sample was treated with BSA (5 mg/ml) in PBS (pH 6.3) for 15 min and then finally rinsed. The cantilever beams used to test for protein attachment in scheme 2 (see Fig. 1b) were treated in a similar manner, except that they did not have the Ab layer attached. Protein attachment scheme 3 (see Fig. 1c) involved treating the cantilevers with biotinylated Ab to vaccinia virus (5 mg/ml) for 15 min and then being rinsed in PBS-Tween 20 (0.05% vol.) for 1 min. All chips were then placed in increasing concentrations of methanol (25% → 50% → 75% → 100%) for ≈1 min each and then dried by using CPD.

Virus Capture Procedure. The antigen mixture (vaccinia virus and adenovirus; ≈10^{11} pfu/ml concentration for each) was allowed to interact with protein-coated cantilever beams for ≈30 min. After this step, they were rinsed in PBS-Tween 20 (0.05%) for 15 min to detach the nonspecifically bound antigens and then rinsed in deionized water for 30 s. They were then immersed in ethanol and dried by using CPD.

1. Ilic, B., Czaplewski, D., Zalautdinov, M., Craighead, H. G., Neuzil, P., Campagnolo, C. & Batt, C. (2001) *J. Vac. Sci. Technol. B.* **19,** 2825–2828.
2. Gupta, A., Akin, D. & Bashir, R. (2004) *Appl. Phys. Lett.* **84,** 1976–1978.
3. Ilic, B., Craighead, H. G., Krylov, S., Senaratne, W., Ober, C. & Neuzil, P. (2004) *J. Appl. Phys.* **95,** 3694–3703.
4. Ilic, B., Yang, Y. & Craighead, H. G. (2004) *Appl. Phys. Lett.* **85,** 2604–2606.
5. Ekinci, K. L., Huang, X. M.H. & Roukes, M. L. (2004) *Appl. Phys. Lett.* **84,** 4469–4471.
6. Yang, Y. T., Callegari, C., Feng, X. L., Ekinci, K. L. & Roukes, M. L. (2006) *Nano. Lett.,* **6,** 583–586.
7. Patolsky, F., Zheng, G., Hayden, O., Lakadamyali, M., Zhuang, X. & Lieber, C. M. (2004) *Proc. Natl. Acad. Sci. USA* **101,** 14017–14022.
8. Chen, G. Y., Thundat, T., Wachter, E. A. & Warmack, R. J. (1995) *J. Appl. Phys.* **77,** 3618–3622.
9. Lee, J. H., Kim, T. S. & Yoon, K. H. (2004) *Appl. Phys. Lett.* **84,** 3187–3189.
10. Pallandre, A., Meersman, B. D., Blondeau, F., Nysten, B. & Jones, A. M. (2005) *J. Am. Chem. Soc.* **127,** 4320–4325.
11. Gupta, A., Akin, D. & Bashir, R. (2005) in *The 18th Annual International Conference on Micro Electro Mechanical Systems* (IEEE, Piscataway, NJ), pp. 746–749.
12. Stryer, L. (1995) *Biochemistry* (Freeman, New York), 4th Ed., pp. 361–390.
13. Peters, T., Jr. (1985) *Adv. Protein Chem.* **37,** 161–245.
14. Hendrickson, W. A., Pähler, A., Smith, J. L., Yoshinori, S. & Merritt, E. A., Phizackerley, R. P. (1989) *Proc. Natl. Acad. Sci. USA* **86,** 2190–2194.
15. Beer, F. P. & Johnston, E. R., Jr. (1981) *Mechanics of Material* (McGraw–Hill, New York), pp. 168–172.
16. Han, W., Mou, J., Sheng, J., Yang, J. & Shao, Z. (1995) *Biochemistry* **34,** 8215–8220.
17. Ptak, A., Takeda, S., Nakamura, C., Miyabe, J., Kagesshima, M., Jarvis, S. P. & Tokumoto, H. (2001) *J. Appl. Phys.* **90,** 3095–3099.
18. Andersson, K. M. & Hovmöller, S. (2000) *Acta. Crystallogr. D* **56,** 789–790.
19. Li, X., Ono, T., Wang, Y. & Esashi, M. (2003) *Appl. Phys. Lett.* **83,** 3081–3083.
20. Wolf, S. & Tauber, R. N. (1986) in *Process Technology*, Silicon Processing for the VLSI Era (Lattice, Sunset Beach, CA), Vol. 1, pp. 647.
21. Ramsden, J. J. (1995) *Chem. Soc. Rev.* **24,** 73–78.
22. Nair, P. R. & Alam, M. A. (2006) *Appl. Phys. Lett.,* **88,** 233120–233123.
23. Walters, D. A., Cleveland, J. P., Thomson, N. H., Hansma, P. K., Wendman, M. A., Gurley, G. & Elings, V. (1996) *Rev. Sci. Instrum.* **67,** 3583–3590.
24. Sader, J. E., Chon, J. W. M. & Mulvaney, P. (1999) *Rev. Sci. Instrum.* **70,** 3967–3969.
25. Huang, T. T., Stugris, J., Gomez, R., Geng, T., Bashir, R., Bhunia, A. K., Robinson, J. P. & Ladisch, M. R. (2003) *Biotechnol. Bioeng.* **81,** 618–624.

APPLIED PHYSICAL SCIENCES

BIOPHYSICS